

RESEARCH ARTICLE

10.1002/2014JC010679

Linkage between lateral circulation and near-surface vertical mixing in a coastal plain estuary

K. D. Huguenard¹, A. Valle-Levinson¹, M. Li², R. J. Chant³, and A. J. Souza⁴

Key Points:

- Near-surface mixing was observed during the ebb phase of the tide
- The mixing was linked to lateral processes, which varied across the estuary
- Near-surface mixing was uncoupled from bottom friction

Correspondence to:

K. D. Huguenard,
Kimberly.huguenard@tamucc.edu

Citation:

Huguenard, K. D., A. Valle-Levinson, M. Li, R. J. Chant, and A. J. Souza (2015), Linkage between lateral circulation and near-surface vertical mixing in a coastal plain estuary, *J. Geophys. Res. Oceans*, 120, 4048–4067, doi:10.1002/2014JC010679.

Received 23 DEC 2014

Accepted 6 MAY 2015

Accepted article online 12 MAY 2015

Published online 7 JUN 2015

¹Department of Civil and Coastal Engineering, University of Florida, Gainesville, Florida, USA, ²Horn Point Lab, University of Maryland Center for Environmental Sciences, Cambridge, Maryland, USA, ³Institute of Marine and Coastal Sciences, Rutgers University, New Brunswick, New Jersey, USA, ⁴National Oceanographic Centre, Liverpool, UK

Abstract Microstructure and current velocity measurements were collected at a cross-channel transect in the James River under spring and neap tidal conditions in May 2010 to study cross-estuary variations in vertical mixing. Results showed that near-surface mixing was related to lateral circulation during the ebb phase of a tidal cycle, and that the linkage was somewhat similar from neap to spring tides. During neap tides, near-surface mixing was generated by the straining of lateral density gradients influenced by the advection of fresh, riverine water on the right side (looking seaward) of the transect. Spring tide results revealed similar findings on the right side of the cross section. However, on the left side, the straining by velocity shears acted in concert with density straining. Weak along-estuary velocities over the left shoal were connected to faster velocities in the channel via a clockwise lateral circulation (looking seaward). These results provided evidence that in the absence of direct wind forcing, near-surface vertical mixing can occur from mechanisms uncoupled from bottom friction.

1. Introduction

The spatial distribution of vertical mixing affects the exchange flow, stratification, residence time, and scalar transport in estuaries [e.g., Geyer *et al.*, 2008]. Vertical mixing can be generated in regions of the water column with increased vertical gradients in horizontal velocity. These vertical gradients are most often found near the bottom, where flow interacts with the boundary, or near the surface, from wind stress. While vertical shears in velocity promote mixing, vertical stratification of water density acts to inhibit it [Turner, 1973]. When compared to stratified and well-mixed estuaries, partially mixed or weakly stratified systems feature the most robust exchange flow, which is driven by horizontal density gradients promoted by vertical mixing. Therefore, it is essential to understand the mechanisms behind vertical mixing at various temporal and spatial scales.

Peters [1997] explored the spring to neap and intratidal variability of vertical mixing in the Hudson River. During neap conditions, the largest vertical eddy diffusivity values occurred at maximum flood, confined to the portion of the water column underneath the pycnocline. However, during spring tides, the largest vertical mixing extended throughout the water column by the end of ebb. The measurements supporting those results were collected over the deepest part (the channel) of the estuary. Collignon and Stacey [2013] built upon those observations by examining the turbulence dynamics at a channel-shoal transition in South San Francisco Bay, under partially mixed conditions. They found enhanced turbulence near the surface during late ebb, influenced by lateral flows. Their analytical framework evaluated various lateral flow mechanisms and their influence on water column stability. Their main findings were that lateral straining of density and velocity shears were the principal water column destabilizers.

The objective of the present investigation was to extend these previous findings in two ways. The first goal was to examine near-surface water column stability across the channel and determine whether the same mechanisms responsible for mixing in the channel extended to the shoals. The second goal was to provide dissipation rates of turbulent kinetic energy (TKE) and values of vertical eddy viscosity derived from microstructure measurements, comparing to the acoustic techniques in Collignon and Stacey [2013]. This investigation demonstrates that near-surface vertical mixing during the ebb phase was indeed linked to lateral circulation. However, the destabilizing mechanisms varied across the estuary. Next, a background on lateral

circulation in partially mixed estuaries is reviewed to lay the foundation for understanding how lateral flows can be linked to near-surface mixing.

1.1. Lateral Circulation

Lateral circulation, sometimes referred to as secondary circulation, describes the across-channel flows that develop in estuaries. These lateral flows are typically smaller than the along-channel component, typically only 10% of the along-channel currents [Lerczak and Geyer, 2004]. However, they can still influence the along-channel dynamics. Lerczak and Geyer [2004] used numerical simulations to show that lateral circulation was about four times stronger during flood tides than ebbs. They indicated a flood/ebb asymmetry that was influenced by tidal variations in stratification and feedback between lateral flows and along-channel dynamics.

There are several mechanisms that govern lateral flows, including Coriolis acceleration, friction, flow curvature, and lateral density gradients [Chant, 2010]. Li et al. [2014] developed a technique to evaluate these mechanisms through the streamwise vorticity. They used numerical simulations in a tidally driven estuarine channel under a variety of conditions to determine the key mechanisms. They found that in estuaries of intermediate widths with Earth's rotational effects, lateral Ekman forcing governed flows in the bottom boundary layer. Lateral Ekman forcing, which represents the tilting of planetary vorticity, induced a one-cell lateral circulation that switched direction with the phase of the tide. The vorticity budget exposed a three way balance among the tilting of planetary vorticity by vertical shear in along-channel currents, lateral baroclinicity, and turbulent diffusion. The lateral circulation varied with estuarine width, producing two counter-rotating cells in dynamically narrow estuaries, and one vortex focused on the left side (looking into the estuary) in dynamically wide estuaries. The observations described in this study are placed in the context of those theoretical findings.

1.2. Study Area

This investigation took place in the James River, which is the southernmost tributary to the largest estuary in the United States, the Chesapeake Bay. The mean annual discharge of the James River in 2010 was $198 \text{ m}^3/\text{s}$, according to the United States Geological Survey. The system is considered a coastal plain estuary with a partially mixed water column [Shen and Lin, 2006], featuring density values that range from 1006 kg/m^3 near the surface to 1018 kg/m^3 near the bottom. Spring tidal amplitudes are approximately 0.45 m, while neap amplitudes are 0.2 m and both primarily semidiurnal. The typical residual circulation is vertically and laterally sheared, featuring landward flow near the bottom in the channel, and seaward flow near the surface and from surface to bottom over shoals [Valle-Levinson et al., 2000]. The Chesapeake Bay region has intermittent pulses of wind lasting 2–7 days [Li et al., 2005]. A seasonal pattern yields dominant southward wind during winter months (November to February) and northward winds during summer months.

During this experiment, the Stokes number, St_k , representing the ratio of friction to local acceleration [e.g., Huijts et al., 2006; Souza, 2013], varied intratidally from <1 to >6 from ebb to flood phases. The James River was observed to be periodically stratified, consistent with an average horizontal Richardson number, Ri_x , of 0.7. However, this value varied above and below 1 throughout the experiment. The James River features a moderate dynamical width and moderate friction. The moderate width is given by a Kelvin number (ratio of basin's width to internal Rossby radius) $K \approx 1$. The moderate friction, in turn, is indicated by an Ekman number (ratio of frictional to Coriolis effects) of $E_k = 0.15$ [Valle-Levinson, 2008]. This study was carried out along a 2 km transect approximately 20 km landward of the mouth (Figure 1a). A cross section looking seaward reveals that the bathymetry consists of a 10 m deep channel bisecting two 4–6 m shoals (Figure 1b). In this cross section, the bathymetry south of the channel features a gently sloping incline that connects the south shoal to the channel.

This presentation begins with an outline of the data collection and processing techniques. Section 3 follows with a description of observations and is divided into *Spring* and *Neap Tide Conditions* subsections. Within each of these subsections, observations exploring vertical mixing are provided showing the lateral variability across the estuary. Also, the competition between stratification and velocity shear is studied through Richardson numbers, where Collignon and Stacey's [2013] analytical framework is used to explore the

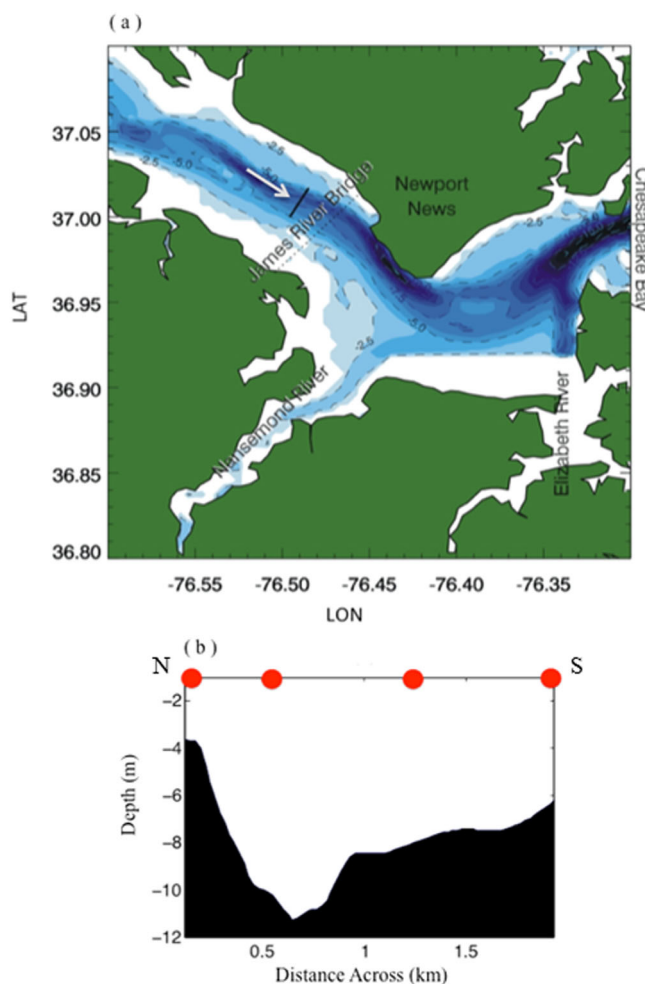


Figure 1. (a) Study area map of the James River. Black line denotes transect, and white arrow represents the perspective of results (i.e., looking seaward). (b) Cross section of transect displaying bathymetry. Red circles represent the four hydrographic station locations.

repeatedly at four locations across the estuary. The instrument descended at 10 cm/s and collected temperature and conductivity measurements at 100 Hz. The four hydrographic stations, denoted by red circles in Figure 1b, were selected to represent two shoals, the deepest section of the channel, and a gently sloping inclination that connected the south shoal to the channel. Hydrographic measurements were collected hourly as the ADCP sampled continuously. The fundamental theory behind the calculation of vertical mixing from the above mentioned measurements is outlined next.

2.1. Mixing Theory

The objective of this study was to ascertain variations in vertical mixing from channel to shoal across an estuary and to determine whether fortnightly variability modulated the distribution. The momentum balance in the along-estuary direction x is:

$$\frac{\partial \bar{u}}{\partial t} + \bar{u} \frac{\partial \bar{u}}{\partial x} + \bar{v} \frac{\partial \bar{u}}{\partial y} + \bar{w} \frac{\partial \bar{u}}{\partial z} - f\bar{v} = -\frac{1}{\rho} \frac{\partial P}{\partial x} - \frac{\partial}{\partial z} (\overline{u'w'}) \quad (1)$$

where x is along-estuary direction, y is across channel, z is vertical, t is time, \bar{u} , \bar{v} , and \bar{w} are the Reynolds-averaged along-channel, cross-channel, and vertical velocity, respectively; f is the Coriolis parameter; ρ_0 is a reference density; P is pressure, and u' and w' are the fluctuating components of along-channel and vertical velocities. The first term on the left-hand side (LHS) of equation (1) represents the local changes in velocity, while the second, third, and fourth terms represent the advective accelerations. The remaining

influence of lateral circulation on water column stability. Vertical mixing results are placed in the context of lateral variability in section 4, after which the main message is presented in section 5.

2. Methods

A field campaign had the purpose of determining the temporal variability in the lateral structure of vertical mixing during a neap and a spring tide in May 2010. Profiles of velocity and hydrography were collected on 5 and 7 May (neap) and 25 and 27 May (spring) 2010, across a 2 km transect for one tidal cycle (~ 12.4 h). Velocity measurements were obtained with a 1200 kHz RDI Acoustic Doppler Current Profiler (ADCP), pointing downward on a 1.2 m catamaran that was towed alongside of a boat at speeds of 1.5–2 m/s. The ADCP sampled at 2 Hz with a 0.25 m vertical resolution ranging from 0.5 to 10 m depth.

In addition to the ADCP, a Self-Contained Autonomous Microstructure Profiler (SCAMP) by Precision Measurement Engineering (PME) was deployed

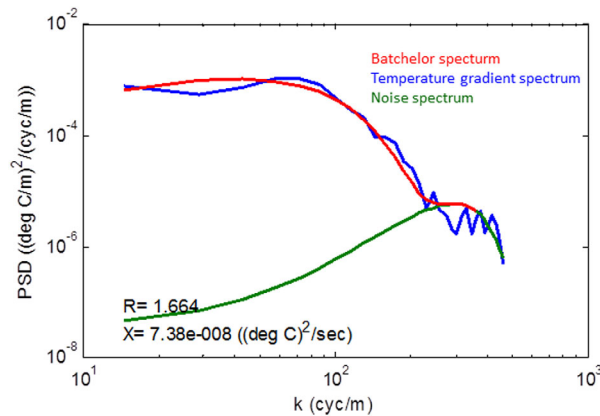


Figure 2. Example fit of the observed temperature gradient (blue) to the Batchelor spectrum (red). Green represents the noise spectrum. χ is the dissipation of temperature variance and R is a spectral fit criterion, where large values (i.e., greater than 3) indicate poor fits.

The Reynolds stresses can be parameterized using a vertical eddy viscosity, A_z , and the vertical gradient in Reynolds-averaged velocity:

$$\overline{u'w'} = -A_z \frac{\partial \bar{u}}{\partial z} \tag{2}$$

The vertical eddy viscosity A_z can be calculated in stratified estuaries [Kay and Jay, 2003] using Osborn's [1980] parameterization, given by the product of a mixing efficiency, m_{ef} , times the ratio of turbulent kinetic energy (TKE) dissipation, ε , to squared vertical shear, $S^2 = (\frac{\partial u}{\partial z})^2 + (\frac{\partial v}{\partial z})^2$:

$$A_z = m_{ef} \frac{\varepsilon}{S^2} \tag{3}$$

Values in the vertical shear estimates that were smaller than the velocity resolution of the ADCP ($\frac{\partial u}{\partial z} < 1 \text{ cm/s} / 25 \text{ cm} < 0.0004 \text{ m/s}$) were removed and linearly interpolated. Estimates of ε (numerator in equation (3)) were obtained from Batchelor fits [Batchelor, 1959]. Following the method of Ruddick et al. [2000], the temperature gradient spectrum was fit to the theoretical Batchelor spectrum, S_B , which is a universal passive scalar spectrum (for an example fit, see Figure 2):

$$S_B(k; k_B; \chi_\theta) = \sqrt{\frac{q}{2}} \chi_\theta k_B^{-1} D_t^{-1} \left(k k_B^{-1} \sqrt{2q} \right) \left[e^{-(k k_B^{-1} \sqrt{2q})^2 / 2} - \int_{(k k_B^{-1} \sqrt{2q})}^{\infty} e^{-x^2 / 2} dx \right] \tag{4}$$

where q is a universal constant taken to be 3.4 [Ruddick et al., 2000], k_B is the Batchelor wavenumber, D_t is the diffusivity of temperature ($1.4 \times 10^{-7} \text{ m}^2/\text{s}$), k is the wave number in rad/m, and χ_θ is the dissipation of temperature variance, which can be determined from integrating the observed temperature gradient spectrum.

Values of k_B were obtained from the fit and used to estimate ε with the molecular viscosity of water, ν :

$$\varepsilon = k_B^4 \nu D_t^2 \tag{5}$$

The fits were conducted using the SCAMP processing software, which implemented a maximum likelihood spectral fitting approach [Ruddick et al., 2000]. Fits were applied to segments consisting of 256 scans, representing $\sim 0.25 \text{ m}$ bin sizes. For details on the uncertainty associated with segment sizes, see Appendix A. Poor fits were identified by large R values (spectral fit criterion outlined in Ruddick et al. [2000]), which occurred before the instrument reached a constant decent rate of $\sim 0.10 \text{ m/s}$. Therefore, measurements collected at depths shallower than 1 m were not usable in estimating ε .

The efficiency of mixing (equation (6)) by a turbulent flow is calculated from the flux Richardson number, R_f .

$$m_{ef} = \frac{1}{1 - R_f} \quad (6)$$

where R_f represents the ratio of the buoyancy term to the shear production term in the TKE budget. The Richardson number (equation (7)) represents the ratio of buoyancy frequency, $N^2 = -g/\rho (\partial\rho/\partial z)$ where ρ is a density, to squared vertical shear (given in equation (3)).

$$R_i = N^2 / S^2 \quad (7)$$

Values of R_f can be estimated by using a turbulent Prandtl number, Pr_t , and Ri (equation (8)).

$$R_f = R_i Pr_t \quad (8)$$

Tjernstrom's [1993] parameterization (equation (9)) was used to estimate a flux Richardson number by determining Pr_t as a function of R_i .

$$Pr_t = (1 + 4.47R_i)^{0.5} \quad (9)$$

When estimating R_i , constraints were taken into consideration regarding the limiting value of Ri . Baumert and Peters [2009] demonstrated that turbulence does not exist when $R_i > 0.5$ because TKE is converted to wave energy. Following the method of Ilıcak et al. [2008], $Pr_t = 10$ was used for all R_i values larger than a less restrictive threshold of $R_i = 1$. Turbulent Prandtl numbers in the present James River investigation were largest (>1) where the water column was stratified, and close to unity near the fully mixed bottom layer. It was assumed that R_f ranged between 0 and 0.19 [Peters et al., 2005]. Provided that stratification in partially mixed estuaries is periodic and varies with depth, the assumption of a constant m_{ef} is unlikely valid. This is why R_f was used to determine m_{ef} . The specifics of data processing are detailed in the next section using the framework for mixing theory outlined above.

2.2. Data Processing

Underway current velocity data were temporally averaged (10 s) to obtain a spatial resolution of 10–20 m. Current velocity data were also rectified from compass errors [Joyce, 1989]. Cross-estuary transects were determined from the beginning and end time of each transect and were interpolated onto a uniform rectangular grid with a vertical resolution of 0.25 m and horizontal resolution of 25 m. Principal component analysis was used to rotate ($\sim 40^\circ$) velocities from an East-West and North-South orientation to along and across-channel components. Velocity time series for each station, corresponding to times when the SCAMP profiler was released, were obtained at distances of 0.12, 0.55, 1.37, and 1.94 km from the northern end of the transect. Vertical gradients in velocity were calculated by vertically differentiating (centered differences) the along and across-channel velocity time series at each station. The raw SCAMP profiles were separated by station and segmented into 30 cm bins. To find the temporal evolution of mixing at each station, vertical eddy viscosity values were calculated with equation (3) and interpolated onto the velocity shear grid. A two-dimensional nearest neighbor filter was applied to smooth the distributions of along and across-channel velocity shears, buoyancy frequency, TKE dissipation, and vertical eddy viscosity at each station.

3. Results

The fortnightly and lateral variability of vertical mixing were explored from a neap and spring tide survey. Hydrographic cross sections were presented for three transect repetitions during both flood and ebb phases (total of six repetitions during a cycle). Time series of TKE dissipation, ϵ , and vertical eddy viscosity, A_z , were displayed for each station and showed near-surface mixing during ebb. These results seemed to link near-surface mixing to lateral flows. The controlling mechanisms of lateral circulation were examined using streamwise vorticity, ω_x . Last, a time scale analysis was used to identify the lateral circulation mechanisms that were contributing to low R_i values.

3.1. Neap Tide—Hydrodynamic Observations

All in situ observations were presented with a seaward facing perspective, where positive along-estuary velocities represented ebb (Figure 1). Likewise, the right side of the cross section indicated the southern shoal. Cross sections were presented initially to show density anomaly, σ_A , along and across-channel flows,

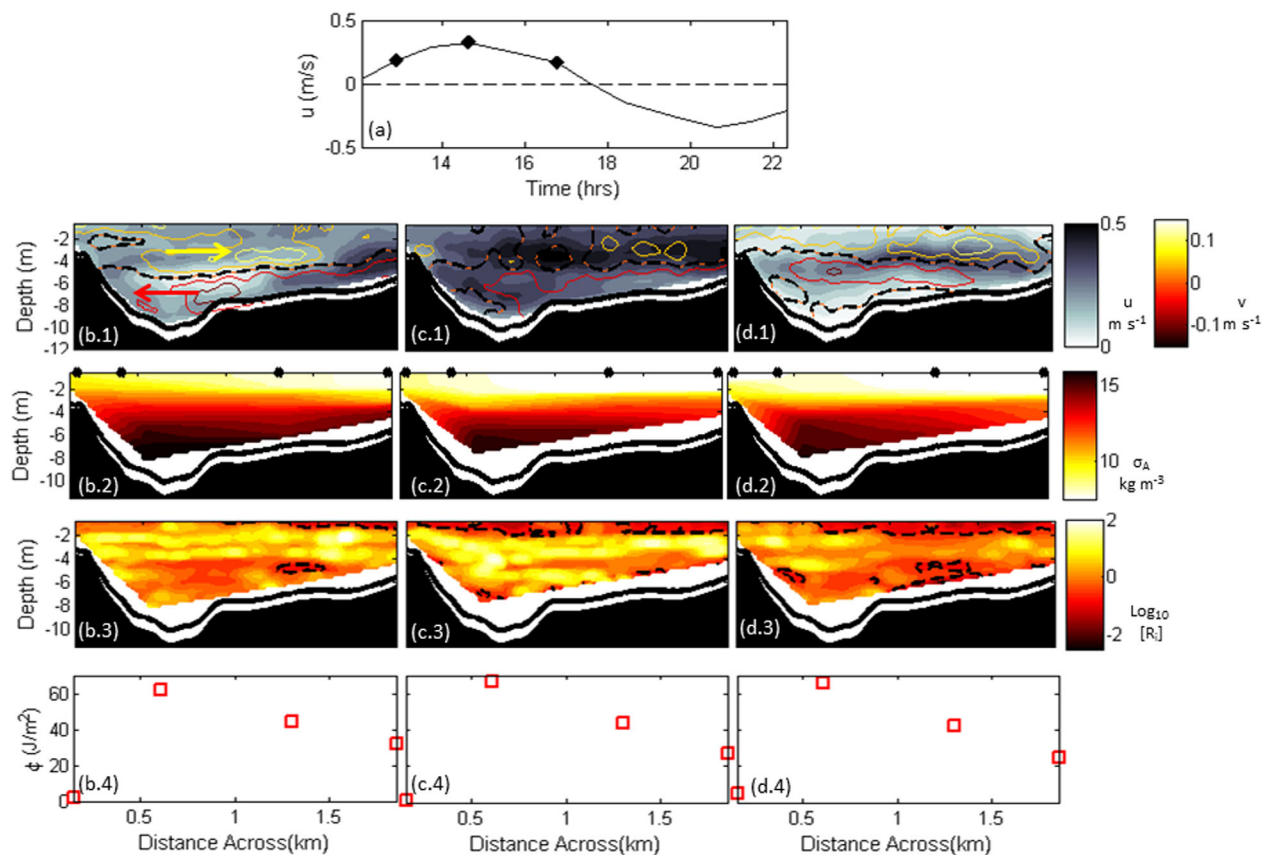


Figure 3. Neap tide cross section for ebb phase (looking seaward): (a) depth-averaged along-channel velocity where red dots depict column (early, peak, late ebb) observations. (b.1–d.1) Gray filled contours depict along-channel flow, while contour lines represent the lateral flows. Black dashed line denotes $v = 0$. Yellow represents the flow to the right (south) and red is flow to the left (north). (b.2–d.2) Density anomaly (density— 1000 kg/m^3). (b.3–d.3) Richardson number contours presented in logarithmic scale. Black dashed line denotes threshold between conditions favorable for mixing and suppression (i.e., $R_i = 0.25$). Darker values (more red) indicate $R_i < 0.25$. (b.4–d.4) Potential energy anomaly, ϕ values for each station.

u and v , Richardson numbers, R_i , and potential energy anomaly, for the beginning of ebb, peak ebb, and end of ebb (Figures 3b.4–3d.4).

3.1.1. Beginning of Ebb

The largest along-channel velocities, u , (0.40 m/s) during the beginning of ebb (Figure 3a, \sim hour13) developed near the bottom over the southern shoal, while the smallest values ($u < 0.10 \text{ m/s}$) appeared middepth between the channel and channel slope (Figure 3b.1). A clockwise, single cell lateral circulation (facing seaward) was characterized by a lower layer of northward v (-0.10 m/s) values below an upper layer of southward v (0.10 m/s) velocities. The interface, defined by 0 m/s v velocities, separated northward from southward flow and corresponded with the depth of the subsurface u minimum velocities.

The spatial structure of density showed the largest values σ_A (15 kg/m^3) in the channel and the smallest σ_A values (7 kg/m^3) in a 2 m layer over channel slope and southern shoal (Figure 3b.2). Correspondingly, the channel displayed the greatest overall water column stratification, with $\phi \sim 60 \text{ J/m}^2$ (Figure 3b.4). The shoals were less stratified, at values of $\phi < 30 \text{ J/m}^2$, while the channel slope displayed moderate stratification ($50 < \phi < 40$). The near-surface advection of relatively fresh water enhanced stratification and was driven by tidal and subtidal velocities that acted in-concert. The freshwater was most prevalent over the southern shoal as influenced by Coriolis acceleration, causing the greatest surface flow to tend to the right. The depth of enhanced stratification, identified by crowded isopycnals, occurred between 4 and 6 m across the transect. This stratified region likely limited near-bottom mixing from influencing the whole water column.

The spatial structure of R_i (Figure 3b.3) showed an unexpected result. Conditions for vertical mixing ($R_i < 0.25$) developed preferably in the upper 2 m of the channel slope and southern shoal. Reduced R_i

values corresponded with the surface layer of freshwater that developed over the southern shoal. The lack of near-bottom $R_i < 0.25$ values was likely influenced by enhanced stratification established in the lower water column. Low R_i values might have existed in the lowermost portion of the water column, which was unresolved by the measurements. The contours are likely influenced by different horizontal resolutions for current velocities and microstructure measurements. The microstructure measurements were much coarser (four locations across the estuary) than velocity measurements (77 profiles across the estuary). More microstructure profiles across the estuary could produce variants from these results.

3.1.2. Peak Ebb

During peak ebb velocities (~hour 15), the largest u values (0.5 m/s) occurred subsurface from the channel to the channel slope (Figure 3c.1) and coincided with the pycnocline depth between 2 and 4 m (Figure 3c.2). While the lateral flow structure still featured near-bottom northward v values, the surface layer was interrupted in the center of the transect. Dense near-bottom σ_A migrated from the channel slope and southern shoal toward the channel. This was identified by less dense water between the channel slope and the southern shoal (Figure 3c.2), compared to the beginning of ebb (Figure 3b.2).

Conditions for mixing occurred in the upper 2 m throughout the transect, except over the channel slope (Figure 3c.3). Stratification increased in the channel, marked by $\phi \sim 70 \text{ J/m}^2$, while the shoals and channel slope featured values similar to the beginning of ebb (Figure 3c.4). Sporadic regions of low R_i values developed in the channel and over the channel slope, indicating conditions for mixing that were influenced by bottom friction from peak along-channel velocities.

3.1.3. End of Ebb

At the end of ebb (~hour 17), reduced u values occurred near the bottom and surface (Figure 3d.1). A three-layered lateral flow structure was related to the transition from clockwise to counterclockwise flow at the bottom. Dense water built up in the channel, while weaker stratification developed over the channel slope and southern shoal (Figure 3d.2), which was evident in R_i values. Conditions for mixing were identified near the bottom over the channel slope and near the surface from the channel to the southern shoal (Figure 3d.3). Low R_i (< 0.25) values appeared near the surface of the southern side of the transect throughout ebb. Conditions during flood were explored at the same cross section during beginning of flood, peak flood, and end of flood.

3.1.4. Beginning of Flood

The beginning of flood (~hour 18) featured the smallest u values at middepth, between the channel and the southern shoal (Figure 4b.1). Everywhere else, flow into the estuary was already well established. The lateral flow structure depicted mainly southward flow throughout the transect, with a thin layer of northward flow at the surface over the channel slope. The spatial structure of σ_A showed dense ocean water in the channel and the remainder of a thin layer of fresher water from ebb confined to the surface of the southern shoal (Figure 4b.2). Smaller velocities during the beginning of flood resulted in $R_i > 0.25$, which indicated hindrance of vertical mixing across the transect (Figure 4b.3). The overall water column stratification was similar to ebb and featured the largest ϕ values (60 J/m^2) in the channel (Figure 4b.4).

3.1.5. Peak Flood

Maximum flood velocities (0.5 m/s) occurred at the surface (Figure 4c.1). A single cell, counterclockwise (facing seaward) lateral circulation featured a 2 m upper layer of northward flow atop a relatively thicker layer of southward flow. Denser water ($> 15 \text{ kg/m}^3$) appeared along the bottom over the southern shoal (Figure 4c.2), than during the beginning of flood (Figure 4b.2). Conditions for vertical mixing were observed at depth in the channel and in a very thin layer $< 1 \text{ m}$ from the channel to the southern shoal (Figure 4c.3). Stratification in the channel reduced to $\phi < 60 \text{ J/m}^2$.

3.1.6. End of Flood

The largest u values at the end of flood (~hour 22) appeared below the surface (Figure 4d.1), influenced by the baroclinic and barotropic pressure gradient forces acting in concert [Lacy *et al.*, 2003]. Southward v values encompassed most of the water column, with a thin layer of northward return flow at the surface. Intermediate density (12 kg/m^3) occupied most of the water column (Figure 4d.2) and the overall stratification was slightly less than in the ebb stage (Figure 4d.4). Conditions for mixing established near the bottom from the channel to the southern shoal from the combined influence of bottom friction and a shallower

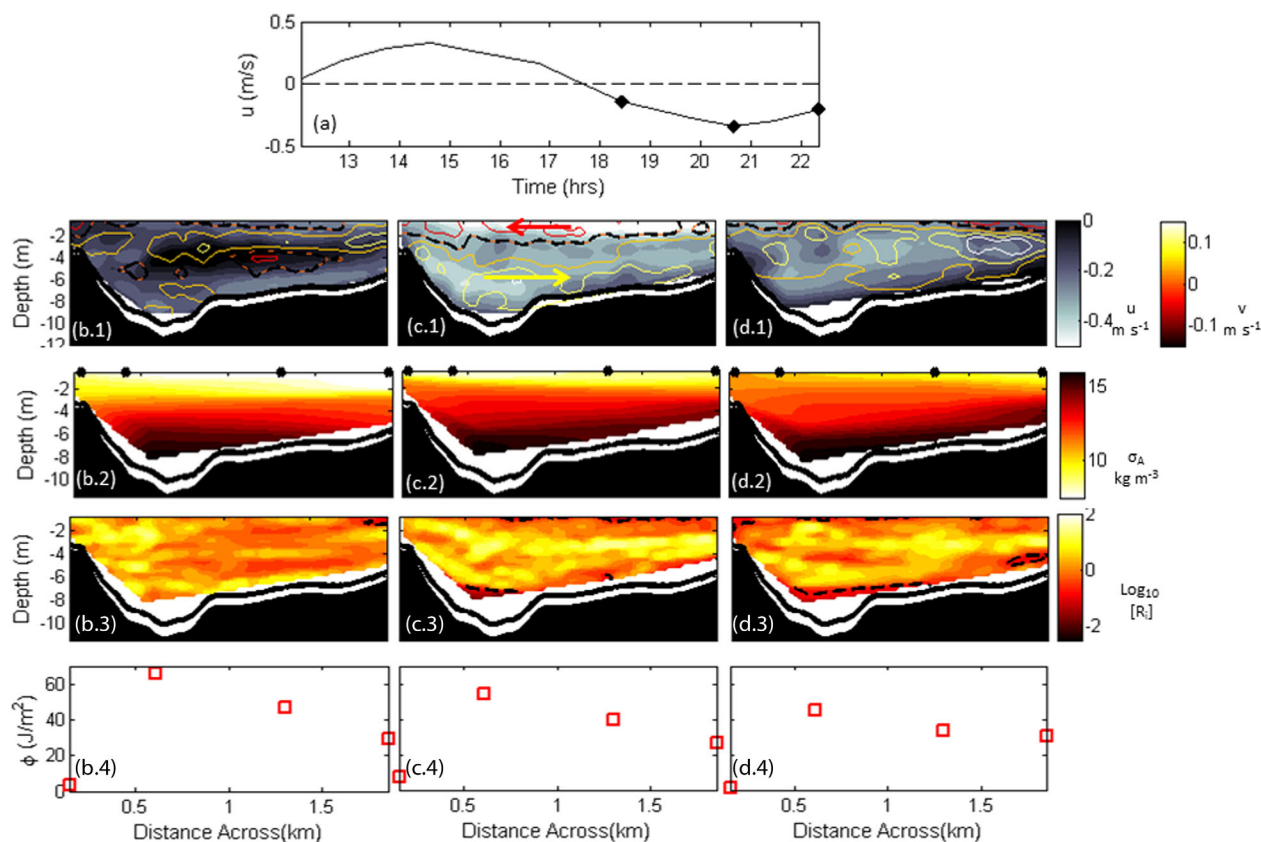


Figure 4. Neap tide cross section for flood phase: (a) depth-averaged along-channel velocity where red dots depict column (early, peak, late flood) observations. (b.1–d.1) Gray filled contours depict along-channel flow, while contour lines represent the lateral flows. Black dashed line denotes $v = 0$. Yellow represents the flow to the right (south) and red is flow to the left (north). (b.2–d.2) Density anomaly (density—1000 kg/m³). (b.3–d.3) Richardson number contours presented in a log base 10 scale. Black dashed line denotes threshold between conditions favorable for mixing and suppression (i.e., $R_i = 0.25$). Darker values (more red) indicate $R_i < 0.25$. (b.4–d.4) Potential energy anomaly, ϕ values for each station.

pycnocline (Figure 4d.3). The overall water column stratification decreased in both the channel and over the channel slope, featuring ϕ values < 50 and < 40 J/m², respectively (Figure 4d.3).

Key findings during neap tide (Figures 3 and 4) included a single-cell lateral circulation that adjusted direction with the phase of the tide. Conditions for mixing developed near the surface during the ebb phase. These conditions were explored further with values of TKE dissipation and vertical eddy viscosity.

3.2. Neap Tide—TKE Dissipation and Vertical Mixing

Time series of squared buoyancy frequency, N^2 , squared vertical shear, S^2 , TKE dissipation, ε , and vertical eddy viscosity, A_z , are shown for each station across the transect to display the lateral and intratidal variability of turbulence and vertical mixing (Figure 5). During ebb (hours 12–18), a well-defined pycnocline was identified by elevated N^2 values (0.03 s^{-2}) between 2 and 4 m depths across the channel, channel slope, and southern shoal (Figures 5d.1–5f.1). Moderate S^2 values (0.012 s^{-2}) developed along the base of the pycnocline in the channel and channel slope, yet elevated values (0.02 s^{-2}) coincided with the depth of the pycnocline over the southern shoal (Figures 5d.2–5f.2). Enhanced ε values ($10^{-5.5}$ – $10^{-6} \text{ m}^2/\text{s}^3$) developed in the upper 2–4 m across the transect and were uncoupled from bottom-related peak ε values ($10^{-5} \text{ m}^2/\text{s}^3$). The near-surface and near-bottom dissipative regions were separated by weaker dissipation ($10^{-7} \text{ m}^2/\text{s}^3$) that was influenced by stratification (Figures 5c.3–5f.3). The greatest A_z values ($10^{-3.5} \text{ m}^2/\text{s}$) were confined (shallower than ε) to a 1–2 m layer across the transect (Figures 5c.4–5f.4), which was detached from 2 m of moderate near-bottom mixing ($10^{-4} \text{ m}^2/\text{s}$).

During the flood stage (hours 18–22), the stratification in the pycnocline reduced to $N^2 \sim 0.02 \text{ s}^{-2}$ and coincided with the location of elevated S^2 values (0.02 s^{-2}). A ε structure similar to ebb was observed, except that the enhanced bottom ε values ($10^{-5} \text{ m}^2/\text{s}^3$) extended higher in the water column (Figures 5c.3–5f.3).

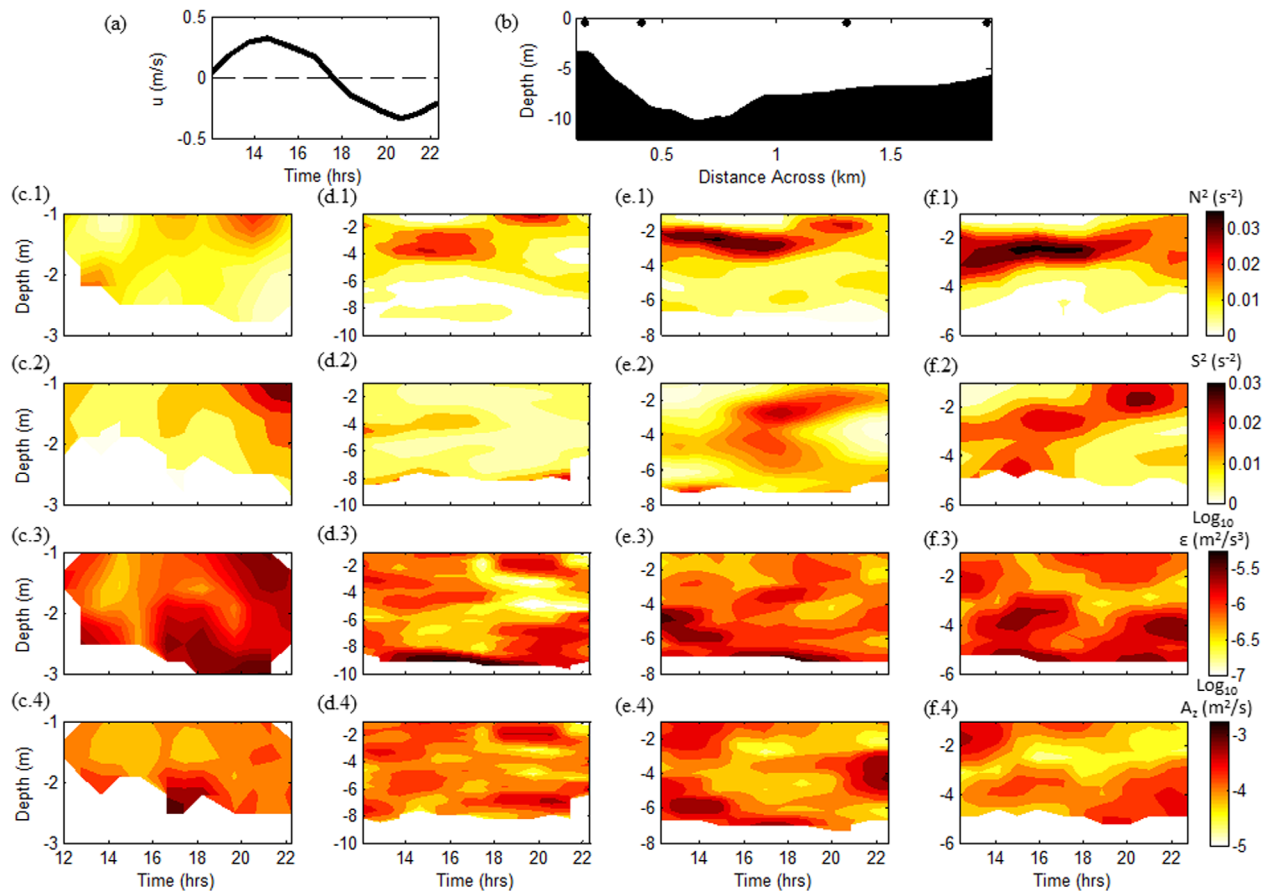


Figure 5. Neap tide: (a) depth-averaged velocity in the channel, positive-ebb, and negative-flood. (b) Cross section displaying station location of each column (b—north shoal, c—channel, d—channel slope, e—south shoal), (c.1–f.1) buoyancy frequency, N^2 , for each station (s^{-2}), (c.2–f.2) squared shear, S^2 , for each station, (c.3–f.3) TKE dissipation, ε at each location, presented in log base 10 scale, (c.4–f.4) vertical eddy viscosity, A_z for each location across the transect, presented in a log base 10 scale.

The near-surface ε during flood did not result in enhanced near-surface A_z over the channel slope and southern shoal. The greatest A_z values were confined to the lowest 2–3 m of the water column. In summary, enhanced ε was observed across the transect throughout the tidal cycle, which was an expected influence of bottom friction. However, elevated ε only induced near-surface mixing during ebb. This is explored in a subsequent section that describes *Collignon and Stacey's* [2013] framework to assess the destabilizing effect of lateral flow mechanisms on water column stratification. This approach quantitatively explores near-surface mixing during ebb. Next, the drivers of lateral flows are examined with the help of streamwise vorticity.

3.3. Neap Tide—Lateral Circulation

The dynamics of lateral circulation were evaluated using along-channel vorticity, $\omega_x = \frac{\partial w}{\partial y} - \frac{\partial v}{\partial z}$, which can be simplified to $\omega_x = -\frac{\partial v}{\partial z}$ because the horizontal length scales are much larger than the vertical length scales, and the vertical flow components are much smaller than the horizontal. The equation for the temporal changes of ω_x consists of a primary balance among tilting of planetary vorticity, baroclinicity, and vertical diffusion [Li *et al.*, 2014]:

$$\frac{d\omega_x}{dt} = f \frac{\partial u}{\partial z} - \frac{g}{\rho} \frac{\partial \rho}{\partial y} + \frac{\partial^2}{\partial z^2} (A_z \omega_x) \quad (10)$$

where ρ is the density. According to Li *et al.* [2014], the first term on the RHS represents generation of along-channel vorticity by lateral Ekman flow (or tilting of planetary vorticity), while the second term is related to lateral density gradients, and the third term is the turbulent diffusion. It was assumed that along-channel changes are negligible, therefore presuming a two-dimensional system where the diffusion term

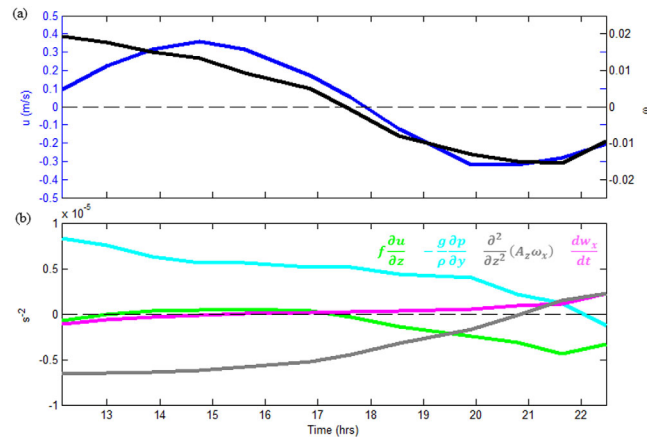


Figure 6. Neap tide: lateral flow mechanisms in terms of streamwise vorticity: (a) depth-averaged velocity—blue (positive—ebb and negative—flood) and streamwise vorticity—black. (b) Green—tilting of planetary vorticity, blue—baroclinicity, red—vertical diffusion, and black—unsteadiness.

can be approximated from the other terms in equation (10). The above terms were cross-sectionally averaged and presented as a time series (Figure 6b). Intratidal variability of the terms was clearly evident. The maximum value of ω_x during ebb was observed in the early stage (at ~ 12 h), which indicated that the lateral circulation was already established. This observation was consistent with lateral flow observations (Figure 3b.1) but inconsistent with the timing of maximum ω_x during flood. The peak value of ω_x during flood was observed at ~ 21.6 h, ~ 1.6 h after maximum flood. During ebb, Ekman forcing (tilting of planetary vorticity), and baroclinicity combined to drive lateral flows and were countered by vertical diffusion and the local changes term. During flood, Ekman forcing dominated the generation of the streamwise vorticity while the lateral baroclinic forcing decreased. Ekman forcing was larger during flood than ebb, suggesting enhanced vertical shear. Greater vertical shear in flood than ebb was an unexpected result and contrary conventional estuarine models [Jay and Musiak, 1994]. During ebb, the largest u velocities actually occurred subsurface, whereas the largest flood velocities occurred at the surface. The distribution was typically reversed, where the largest values were subsurface during flood and near-surface during ebb. Therefore, when the along-channel vertical shear was depth averaged, the result was relatively small because of negative over positive shear associated with the subsurface maximum. These findings were supplemented by a time scale approach to determine the influence of temporally variable lateral flow mechanisms on water column stability near the surface and is discussed next.

3.4. Neap Tide—Time Scale Analysis

A time scale analysis determined the relative influence of four lateral flow mechanisms on the stability of the water column [Collignon and Stacey, 2013]. Their analysis also involved the along-estuary vorticity component ω_x , but in terms of the temporal evolution of the Richardson number R_i (see Collignon and Stacey [2013] for the derivation of equation (11)):

$$\frac{\partial R_i}{\partial t} = \frac{1}{S^2} \left[\omega_x \left(-\frac{g}{\rho_0} \frac{\partial \rho}{\partial y} \right) + \omega_x \left(-2R_i \frac{\partial u}{\partial z} \frac{\partial u}{\partial y} \right) + \omega_x \left(2R_i \frac{\partial u}{\partial z} f \right) + \omega_x \left(-2R_i \frac{\partial \omega_x}{\partial t} \right) + R \right] \quad (11)$$

where S^2 is the amplitude of the squared vertical shear of u and v (i.e., the denominator of R_i); ω_x is represented as the negative vertical gradient of v ; and R is a remainder term not involving ω_x . The terms within the square brackets represent the contribution to R_i from density straining (first term), lateral straining of along-channel velocity shears (second term), Coriolis forcing (third term), and unsteadiness (fourth term). All terms on the RHS of (11) are associated with lateral circulation. Equation (11) can be used to quantify the relative importance of the mechanisms destabilizing the water column. Instead of evaluating the terms directly, Collignon and Stacey [2013] quantified time scales, τ , of the four characteristic processes (the four terms outlined above) and compared them to each other:

$$\tau_\rho = \frac{S^2}{\omega_x \left(-\frac{g}{\rho_0} \frac{\partial \rho}{\partial y} \right)} \quad (12)$$

$$\tau_u = \frac{S^2}{\omega_x \left(-2R_i \frac{\partial u}{\partial z} \frac{\partial u}{\partial y} \right)} \quad (13)$$

$$\tau_f = \frac{S^2}{\omega_x (2R_i \frac{\partial u}{\partial z} f)} \quad (14)$$

$$\tau_t = \frac{S^2}{\omega_x (-2R_i \frac{\partial \omega_x}{\partial t})} \quad (15)$$

where τ_ρ is the time scale associated with the lateral straining of density by the lateral circulation; τ_u is the lateral straining of vertical shears in horizontal velocities; τ_f is Coriolis forcing and represents the conversion of longitudinal vorticity to lateral vorticity; and τ_t is the unsteadiness term evaluating the effect of temporal variations of lateral circulation. A positive time scale value represents a process that stabilizes the water column (increases R_i), while a negative value indicates mixing by decreasing R_i . Each time scale (in hours) is compared to half of the semidiurnal tidal period. Therefore, values greater than 6.2 h have lesser influence than values shorter than half a period. This analysis was performed from the channel to the southern shoal, resulting in time scales between the channel and channel slope and between the channel slope and southern shoal. The time scales were depth averaged over the near-surface mixed layer during ebb (i.e., upper 2.5 m). The orientation used for this analysis was consistent with Collignon and Stacey [2013], where positive indicated upward and to the right (south).

Time scales between the channel (Figure 7b) and channel slope (Figure 7c) during the beginning of ebb (Figure 7a) showed that the straining of lateral density gradients initially (hours 12–13) destabilized the surface region. During this time, fresh riverine water was introduced from the southern shoal to the channel slope, which initially stratified the water column near the surface and set up a lateral density gradient that forced flow toward the south. The lateral flow structure revealed that the fastest southward lateral flows occurred at the surface (Figure 3b.1). Therefore, denser water from the channel was transported by the combined influence of the lateral density gradient and lateral circulation over fresher water in the upper 2 m of the southern side. This resulted in local mixing at the surface, even though freshwater was skewed to the southern half of the cross section by Coriolis deflection and initially acted to stratify the water column. An example capturing this local mixing occurred for the second transect near hour 13, where density anomaly values averaged between the channel/channel slope (Figure 7d) and channel slope/southern shoal (Figure 7e) displayed denser values in the upper 1 m of the water column beneath less dense values. Local mixing was a feature exclusive to ebb phases. During the second transect repetition (hour 13), the Coriolis term and the lateral straining of density gradient term acted in concert to induce mixing. At peak ebb velocities (around 14.5 h), the lateral circulation was disrupted in the surface layer (Figure 3b.1), when vertical diffusion transitioned from driving lateral flows to countering the driving forces, i.e., baroclinicity and Ekman forcing (Figure 7b). This competition effectively inhibited the density straining and Coriolis terms from inducing mixing near the surface, which was indicated by the absence of negative density straining values at 14.5 and 15.5 h. Unsteadiness from the lateral circulation disruption (observable during peak ebb in Figure 3c.1) was the only mechanism inducing near-surface mixing. In late ebb (>hour 16.5) after the lateral circulation spun-up again, the density straining and unsteadiness terms favored mixing at the surface.

Between the channel slope and southern shoal, the behavior was less complicated. During the first half of ebb, density straining induced near-surface mixing (Figure 7c). At peak ebb, when the along-channel velocities were largest, the Coriolis term destabilized the near-surface region. Similar to between the channel and channel slope, both unsteadiness and density straining supported low R_i values in the surface region.

Neap tide results revealed that near-surface vertical mixing developed during ebb and was linked to lateral circulation. The straining of lateral density gradient chiefly acted to destabilize the surface region, which was linked to the along-channel advection of freshwater over the southern half of the transect during ebb. A question that arose was whether near-surface mixing also appeared during ebb spring tide. This was explored next.

3.5. Spring Tide—Hydrodynamic Observations

3.5.1. Beginning of Flood

The along-channel velocities associated with spring tide conditions were greater than during neap and the largest values ($u \sim -0.60$ m/s) were subsurface across the transect (Figure 8b.1). The lateral circulation was counterclockwise (looking seaward), which transported dense water from the channel along the bottom toward the southern shoal. The density anomaly range was smaller during spring tide than in neap tides.

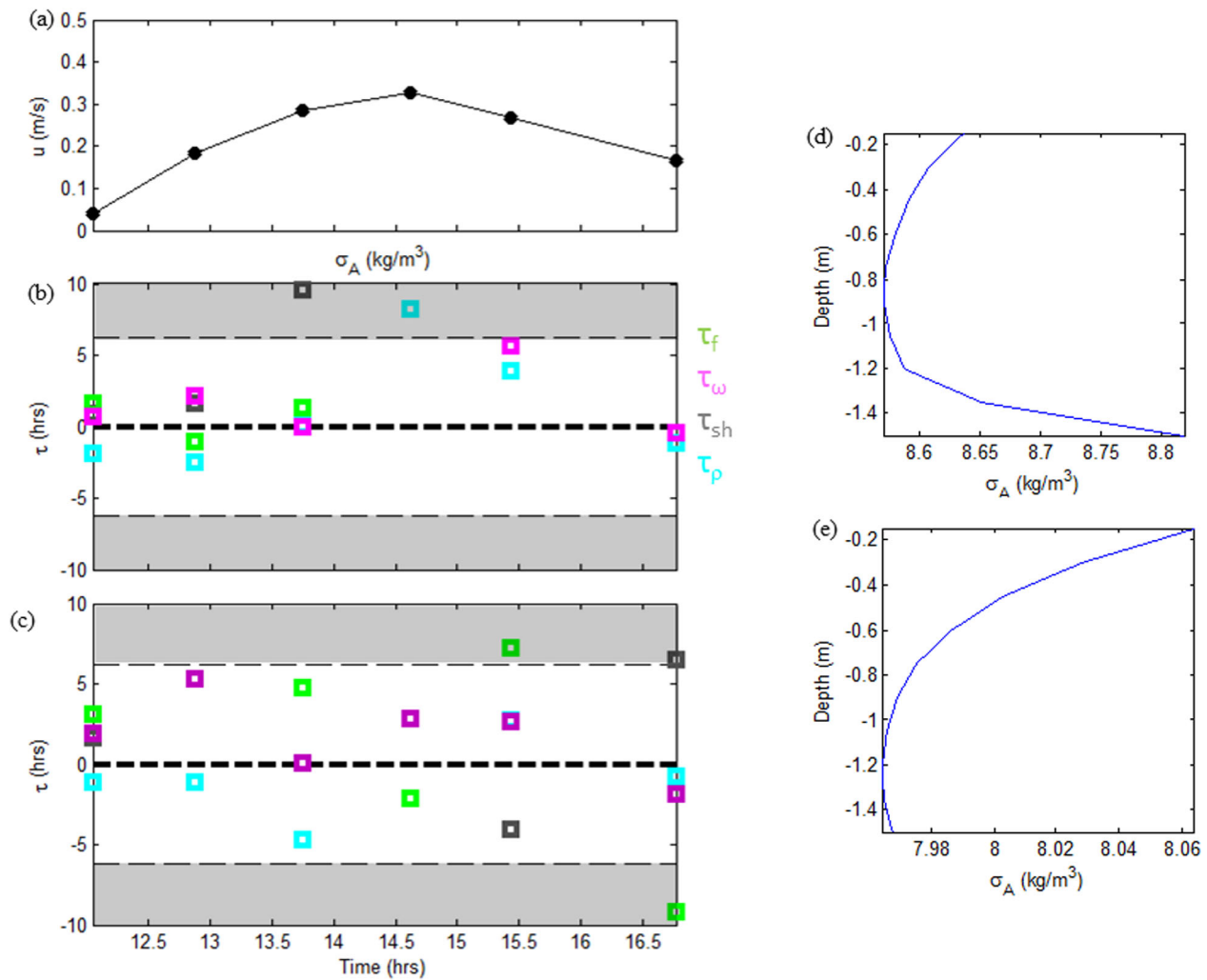


Figure 7. Neap tide time scale analysis for ebb: (a) depth-averaged velocity, red dots denote transects. (b) Between channel and channel slope. Blue—straining of lateral density gradients, red—straining of velocity gradients, black—unsteadiness and green—Coriolis forcing. (c) Between channel slope and southern shoal. Gray boxed denote less important time scales (i.e., >6.2 h). Positive stabilizes the water column while negative destabilizes. (d and e) Surface density anomaly between channel/channel slope and channel slope/southern shoal, respectively, during transect repetition 2 near hour 13.

The greatest densities ($\sigma_A = 12 \text{ kg/m}^3$) occurred in the channel, while the smallest values ($\sigma_A = 8 \text{ kg/m}^3$) developed at the surface of the southern shoal (Figure 8b.2). An overall reduction in stratification was also identified in smaller ϕ values (Figure 8b.4). The greatest stratification was found in the channel, however, markedly smaller than during neap tide ($\phi < 20 \text{ J/m}^2$). Values of R_i showed conditions favorable for mixing ($R_i < 0.25$) confined to the near-bottom region over the northern shoal and channel (Figure 8b.3).

3.5.2. Peak Flood

The largest u values ($\sim -0.75 \text{ m/s}$) were again observed subsurface and corresponded with the depth of the interface of the counterclockwise lateral circulation (Figure 8c.1). Dense σ_A water ($\sim 12 \text{ kg/m}^3$) was transported toward the southern shoal, while fresher waters at the surface ($\sigma_A = 8 \text{ kg/m}^3$) were advected from the southern shoal toward the channel (Figure 8c.2). This was observed in ϕ values, which depicted a marginal increase in the channel (Figure 8c.4). Low R_i values developed in the lower region of the water column across the transect, likely an influence of velocity shears from the enhanced tidal velocities interacting with the bottom (Figure 8c.3).

3.5.3. End of Flood

Along-channel velocities by the end of flood were quite weak ($u < -0.10 \text{ m/s}$) (Figure 8d.1). Dense σ_A values encompassed most of the transect, ranging from 9 to 11 kg/m^3 top to bottom across the transect, which

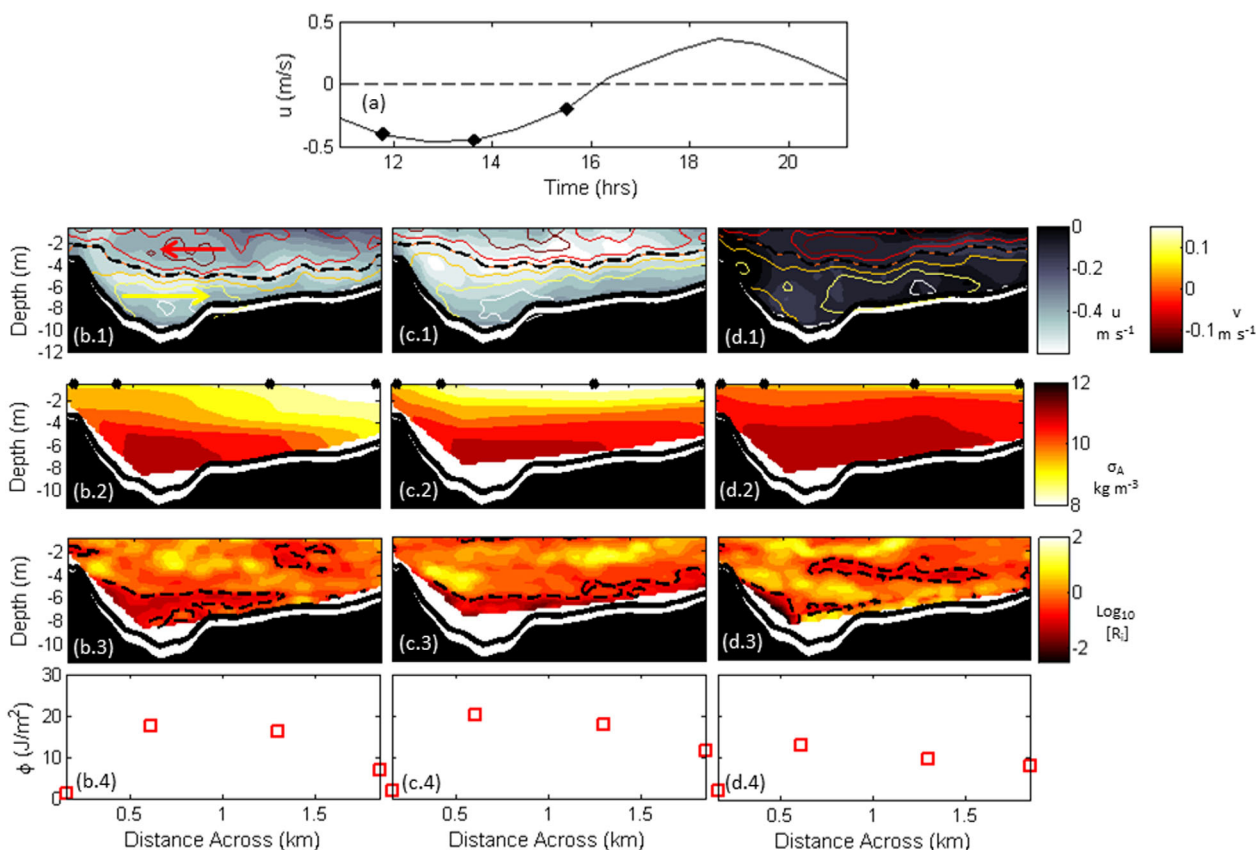


Figure 8. Spring tide cross section for flood phase: (a) depth-averaged along-channel velocity where red dots depict column (early, peak, late flood) observations. (b.1–d.1) Gray filled contours depict along-channel flow, while contour lines represent lateral flows. Black dashed line denotes $v = 0$. Yellow represents flow to the right (south) and red is flow to the left (north). (b.2–d.2) Density anomaly (density—100 kg/m³). (b.3–d.3) Richardson number contours presented in log 10. Black dashed line denotes threshold between conditions favorable for mixing and suppression (i.e., $R_i = 0.25$). Darker values (more red) indicate $R_i < 0.25$. (b.4–d.4) Potential energy anomaly, ϕ values for each station.

was also represented by reduced ϕ values in the channel and channel slope (Figure 8d.4). Favorable conditions for mixing developed near the bottom of the channel, shoals, and middepth over the channel slope (Figure 8d.3).

3.5.4. Beginning of Ebb

The along-channel velocities (Figure 9b.1) at the beginning of ebb (hour ~17.5) showed the greatest values at the surface ($u \sim 0.60$ m/s), in contrast to the subsurface maxima observed during neap tides. A clockwise lateral circulation, in the initial stages of development, featured northward flow in the lower water column of the channel and in the whole water column over the southern shoal. A thin, subsurface region of southward velocities extended from the northern shoal to the channel slope. The spatial structure of density showed the densest values ($\sigma_A \sim 12$ kg/m³) along the bottom of the southern shoal, channel slope, and channel, which drew a lateral density gradient in the lower layer (Figure 9b.2). However, the lightest water ($\sigma_A \sim 8$ kg/m³) appeared at the surface over the southern shoal in a manner similar to that observed during neap tide conditions. Low R_i values occurred near the bottom and middepth in the channel and over the southern shoal (Figure 9b.3). A thin region of $R_i < 0.25$ was found at the surface over the channel slope, which differed from the low R_i values that spanned from the channel slope to the southern shoal during neap tide. Greatest values of stratification ($\phi = 15$ J/m²) were found in the channel, over the channel slope, and over the southern shoal (Figure 9b.4). These values were almost 1 order of magnitude smaller than in neap tides.

3.5.5. Peak Ebb

The largest along-channel ebb velocities ($u \sim 0.7$ m/s) appeared over the southern half of the cross section. A clockwise lateral circulation featured northward velocities below a 2–4 m layer of southward surface flow (Figure 9c.1). The dense values that were previously observed along the bottom from the southern shoal to

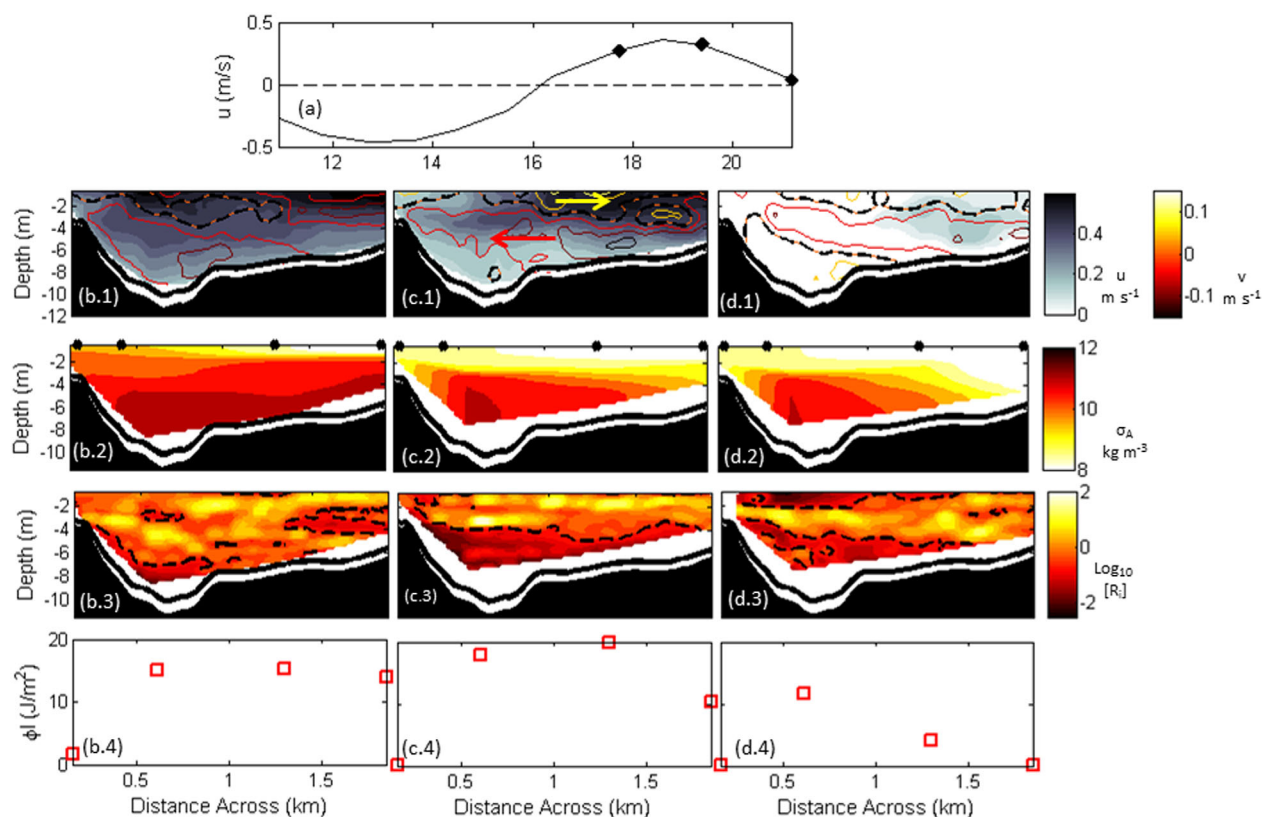


Figure 9. Spring tide cross section for ebb phase: (a) depth-averaged along-channel velocity where red dots depict column (early, peak, late ebb) observations. (b.1–d.1) Gray filled contours depict along-channel flow, while contour lines represent lateral flows. Black dashed line denotes $v = 0$. Yellow represents flow to the right (south) and red is flow to the left (north). (b.2–d.2) Density anomaly (density—100 kg/m³). (b.3–d.3) Richardson number contours presented in a log base 10 scale. Black dashed line denotes threshold between conditions favorable for mixing and suppression (i.e., $R_i = 0.25$). Darker values (more red) indicate $R_i < 0.25$. (b.4–d.4) Potential energy anomaly, ϕ values for each station.

the channel were restricted to the channel (Figure 9c.2). The surface region of freshwater encompassed most of the cross section from the southern shoal to the channel slope. Increased values of ϕ displayed the greatest stratification (20 J/m²) over the channel slope, which was influenced by the lateral advection of freshwater toward the north (Figure 9c.4). Conditions favorable for mixing developed near the bottom across the transect, throughout the water column over the northern shoal, and in a thin surface layer over the southern shoal (Figure 9c.3).

3.5.6. End of Ebb

At the end of ebb, along-channel velocities were weak ($u < 0.20$ m/s) and the lateral circulation was three layered (Figure 9d.1). Low-density values ($\sigma_A \sim 8$ kg/m³) were observed over the southern shoal and along the surface in the channel and channel slope (Figure 9d.2). Most notable was that low R_i values developed in a 2 m layer at the surface across the transect. The surface layer was separated from the bottom mixed layer by the pycnocline (Figure 9d.3). The mixing at the surface resulted in overall low ϕ values (< 15 J/m²) across the transect (Figure 9d.4).

Spring tide conditions during the ebb phase of the tide varied from the neap tide observations. While conditions favorable for mixing were observed near the surface during both spring and neap ebbs, low R_i values developed in late ebb during the spring tide survey. Time series of TKE dissipation and vertical eddy viscosity were next compared to the low R_i values observed during late ebb.

3.6. Spring Tide—TKE Dissipation and Vertical Mixing

During flood, stratification was weak, as indicated by uniform $N^2 < 0.05$ s⁻² and no visible pycnocline (Figures 10c.1–10f.1). Elevated S^2 values (10⁻² s⁻²) were observed along the bottom as well as in a 4 m surface layer across the transect (Figures 10c.2–10f.2). The largest ε values (10^{-4.5} m²/s³) were confined to the bottom during peak velocities in the channel (Figure 10d.3), and channel slope (Figure 10e.3). Values of

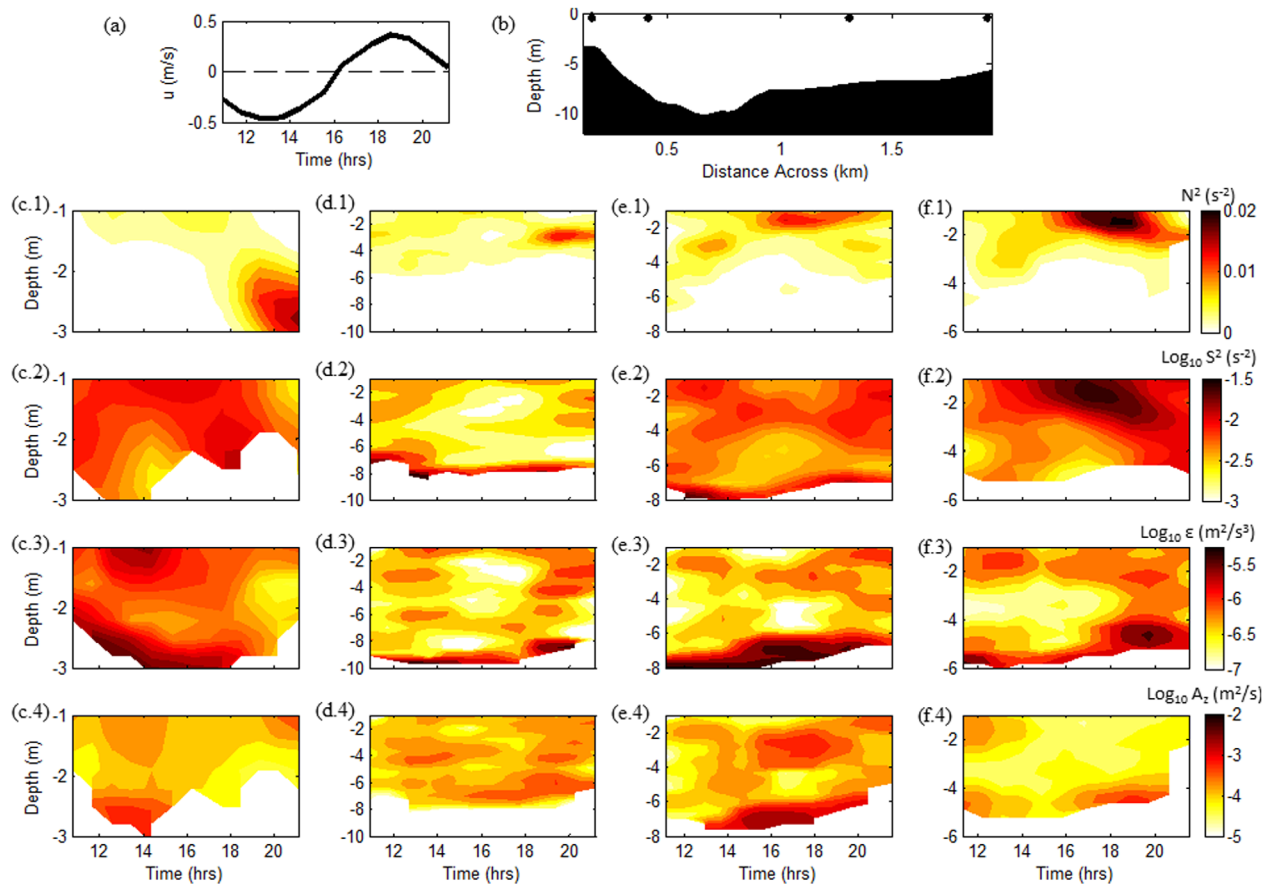


Figure 10. Spring tide: (a) depth-averaged velocity in the channel, positive-ebb, and negative-flood. (b) Cross section displaying station location of each column (b—north shoal, c—channel, d—channel slope, e—south shoal), (c.1–f.1) buoyancy frequency, N^2 , for each station (s^{-2}), (c.2–f.2) squared shear, S^2 , for each station, (c.3–f.3) TKE dissipation, ε at each location, presented in log base 10 scale, (c.4–f.4) vertical eddy viscosity, A_z for each location across the transect, presented in a log base 10 scale.

order $10^{-6} \text{ m}^2/\text{s}^3$ were observed near the surface across the transect during peak flood at hour 14 (Figures 10c.3–10f.3). Vertical eddy viscosity values were greatest near the bottom after peak flood, featuring $A_z \sim 10^{-3} \text{ m}^2/\text{s}$. Over the channel slope (Figure 10e.4) and southern shoal (Figure 10f.4), moderate A_z values ($10^{-4} \text{ m}^2/\text{s}$) developed subsurface at 2 m depths from hours 11 to 14.

During ebb (hours 16–21), a pycnocline was identified near the surface of the southern half of the transect and featured moderate stratification ($N^2 \sim 0.01$ to 0.02 s^{-2}). Enhanced S^2 values (10^{-2} s^{-2}) developed throughout most of the water column over the northern shoal, channel slope, and southern shoal (Figures 10c.2, 10e.2, and 10f.2), yet were confined to near-bottom and near-surface regions in the channel (Figure 10d.2). The structure of ε during ebb featured a similar distribution as flood, where the largest values were confined near the bottom of the channel, channel slope, and southern shoal during peak velocities at hours 18–20. Moderate values appeared at the surface of the channel, channel slope, and southern shoal throughout the ebb phase. The vertical eddy viscosity showed two regions of enhanced vertical mixing across the transect near the surface and bottom during the second half of ebb. The surface layer featured $A_z \sim 10^{-3}$ in the upper few meters across the transect, which was consistent with R_i findings.

3.7. Spring Tide—Lateral Circulation

The maximum cross-sectionally averaged streamwise vorticity appeared ~ 1 h after peak flood velocities (Figure 11a). During ebb, ω_x attained a maximum later in the tidal stage, approximately 2 h after peak flows. The vorticity analysis showed that the tilting of planetary vorticity (Ekman forcing) generated streamwise vorticity during flood but was most prominent during ebb, which was expected because of the enhanced vertical shears from maximum near-surface ebb velocities. This varied from the neap lateral circulation pattern, which showed reduced Ekman forcing from the subsurface velocity maximum influenced small depth-

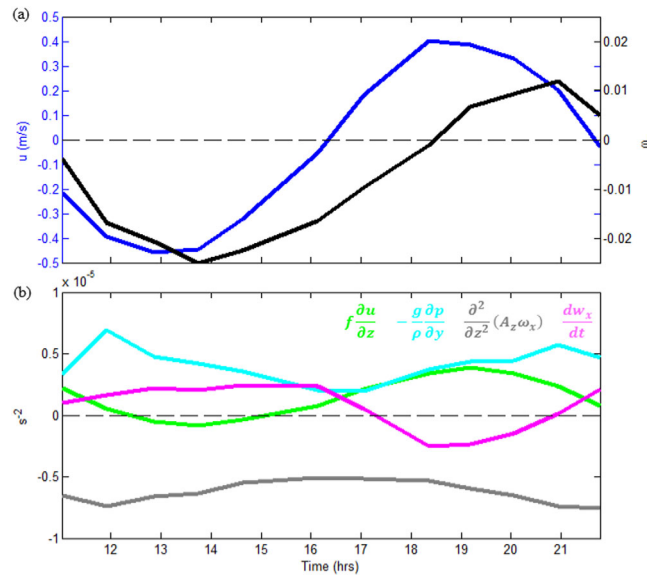


Figure 11. Spring tide: lateral flow mechanisms in terms of streamwise vorticity: (a) depth-averaged velocity—blue (positive—ebb and negative—flood) and streamwise vorticity—black. (b) Green—tilting of planetary vorticity, blue—baroclinicity, red—vertical diffusion, and black—unsteadiness.

(looking seaward), resulting in downward sloping isopycnals throughout the tidal cycle. This results in positive lateral baroclinicity regardless of the tidal phase.

3.8. Spring Tide—Time Scale Analysis

None of the lateral flow mechanisms acted to destabilize the surface layer between the channel and channel slope during the beginning of ebb (Figure 12b). At peak ebb velocities, unsteadiness supported low R_i

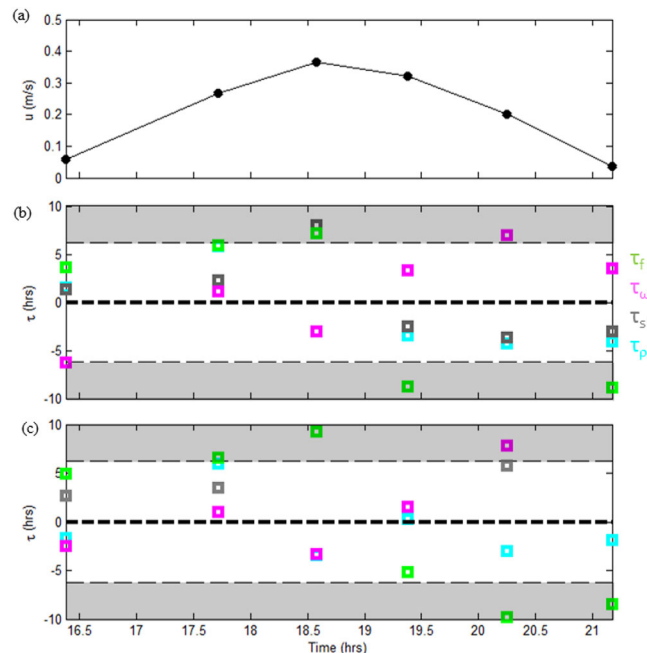


Figure 12. Spring tide time scale analysis for ebb: (a) depth-averaged velocity, red dots denote transects. (b) Between channel and channel slope. Blue—straining of lateral density gradients, red—straining of velocity gradients, black—unsteadiness, and green—Coriolis forcing. (c) Between channel slope and southern shoal. Gray boxed denote less important time scales (i.e., >6.2 h). Positive stabilizes the water column while negative destabilizes.

averaged vertical shears. The lateral baroclinicity forcing remained positive since there is a strong rotational control under the weak stratification and the isopycnals are tilted downward on the southern shoal throughout the flood-ebb tidal cycle. Vertical diffusion opposed baroclinicity.

During ebb, the Ekman forcing and baroclinicity drove lateral flows and were countered by local changes and vertical diffusion. These results were consistent with the results of the widest channel run ($K \sim 1.1$) in Li *et al.* [2014], where the influence of Coriolis forcing was dominant. Similar to the observations in the present study, the lateral density structure depicted fresh-water confined to the right

values because the streamwise vorticity switched direction (Figure 10a). Density straining combined with the lateral straining of velocity shears to induce mixing. The lateral straining of velocity shears influenced a sub-surface u maximum, which was evident in the channel during peak ebb (Figure 9c.1). The sub-surface maximum was induced by the lateral circulation, which featured the strongest lateral flows at the surface. Surface lateral flow decreased with depth to the interface of the lateral circulation. Lateral flow at the surface linked the slower water from the northern shoal, influenced by the shallow bathymetry over faster flow in the channel.

The combination of the lateral flows and shallowness at the northern shoal imposed a

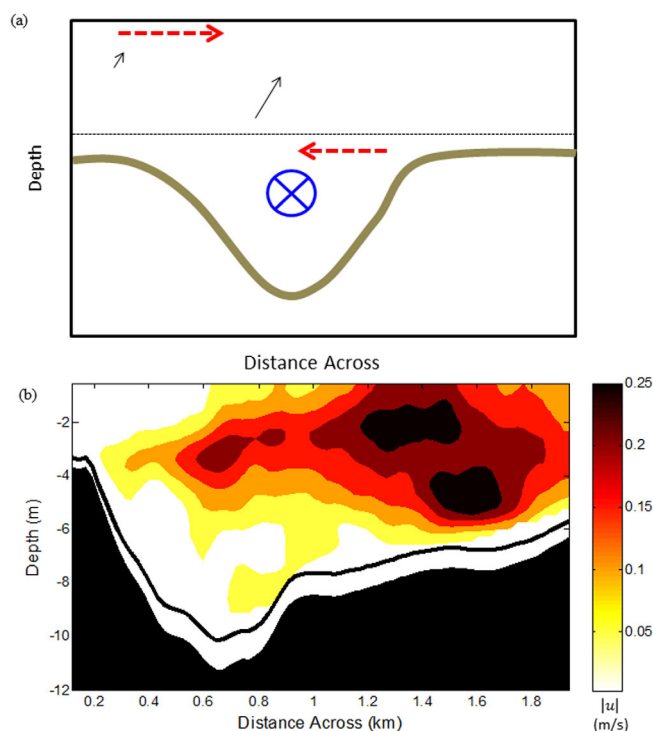


Figure 13. (a) Schematic detailing velocity shear straining. Red dashed arrows represent the lateral flow, while blue circle denotes along-channel flow into the page. Black arrows show velocity magnitude which rotates in direction with depth and highlights vertical shear in horizontal velocities that is generated by lateral flows. (b) Ebb phase velocity magnitude from \sim hour 20 on 27 May during spring tide conditions. Flow is going into the page (facing seaward).

vertical shear in the surface region, which is characterized schematically in Figure 13a. This was evident in spring tides late in the ebb phase (\sim hour 20) on 27 May (Figure 12b). Slower flow (<0.05 m/s) from the northern shoal extended along the surface to the channel and was located over faster subsurface flow (~ 0.20 m/s). The change in velocity magnitude toward the surface represents how the lateral straining of velocity shear destabilized the water column. Similar to neap tide observations, a lateral density gradient developed near the surface from the freshwater that was skewed on the southern side by Coriolis forcing. Even though the freshwater appeared on the southern side initially stratified the near-surface region, denser water was transported over the light water near the surface by lateral flows, which resulted in local density inversions.

Between the channel slope and southern shoal, unsteadiness promoted low R_i values at peak (hour 18.5) velocities, similar to the channel/channel slope observations (Figures 12b and 12c). After peak velocities, density straining was the main contributor to near-surface instabilities. These results showed that near-surface mixing was linked to lateral circulation, and that the mechanisms responsible for inducing mixing varied in space and time. Intratidal, fortnightly, and spatial variability of these fields, along with the most relevant findings and their implications are considered next.

4. Discussion

This study compares the lateral variability of vertical mixing from spring to neap tides. The key and most innovative finding was that vertical mixing developed near the surface during the ebb phase and was influenced by lateral processes. During neap tide, the water column was more stratified than during spring tide and tidal velocities were weaker. A single-cell lateral circulation developed and changed direction with the phase of the tide. A vorticity analysis, used to evaluate mechanisms contributing to lateral circulation, presented a complex cross-sectional balance during ebb. During this phase, Ekman forcing and lateral baroclinicity drove streamwise vorticity, while vertical diffusion and unsteadiness acted to spin down vorticity. These processes changed during the spring ebb tide, when Ekman forcing was larger and lateral baroclinicity remained positive for the entire survey. The underlying difference was that the ω_x was not already established at the beginning of spring tide ebb of the spring tide in contrast to the neap tide ebb. In consequence, near-surface mixing developed later in the spring ebb phase. This was also observed in the lateral circulation, which changed direction ~ 2 h after the along-channel velocity transitioned to the ebb direction.

A characteristic time scale approach was implemented to evaluate lateral circulation effects on near-surface stability. Results revealed that the principal mechanism destabilizing the water column near the surface (from the channel to the southern shoal during the ebb phase of the neap tide) was the straining of lateral

density gradients. Coriolis acceleration forced relatively fresher water at the surface, but was confined over the southern shoal, which set up a near-surface lateral density gradient that acted in concert with lateral flows. Therefore, the lateral flows transported denser water from the northern side of the transect along the surface toward the southern shoal. A statically unstable water column developed from the channel toward the southern shoal and was specific to ebb.

Vertical mixing developed near the surface during the ebb phase of the spring tide, but it was most prevalent during late ebb rather than throughout the tidal cycle. The time scale analysis showed that between the channel and channel slope, the straining of lateral density gradients combined with the straining of velocity gradients to destabilize the water column. Straining of velocity shears developed from the influence of lateral flows at the surface, which induced vertical shear in horizontal flows. The associated vertical shears in velocity that developed, highlighted by a subsurface maximum, acted to destabilize the water column. Though the same lateral circulation was present during neap, the enhanced stratification suppressed any local mixing that could have developed from shear straining. From the channel slope to the southern shoal, only the straining of lateral density gradients resulted in instabilities at the surface.

In a channel-shoal section in South San Francisco Bay, *Collignon and Stacey* [2013] indicated increased shear production at the surface and increased depth-averaged TKE dissipation late in the ebb phase of the tidal cycle. They suggested that the surface turbulence was being generated by lateral circulation. Their time scale approach, implemented in the present research, revealed that the straining of lateral density gradient and velocity shear were the chief drivers for destratifying the water column. Those findings complement part of the main message of this investigation in the James River. While the same mechanisms were determined here to destratify the water column during late ebb spring between the channel and channel slope, this study also showed fortnightly and lateral variability. Between the southern shoal and channel slope, only the straining of lateral density gradients influenced near-surface mixing. Also, only density straining promoted mixing between the channel and channel slope during neap tide. This was different from *Collignon and Stacey's* [2013] findings, whose observations were collected during spring tide and depicted the combined influence of lateral straining of density and velocity shear. The similar findings imply that late ebb near-surface mixing likely occurs in other partially mixed estuaries.

Overall, this study has shown that the mechanisms contributing to near-surface mixing vary from neap to spring tide and across the transect, which adds another layer of complexity to *Collignon and Stacey's* [2013] findings. The near-surface mixing is uncoupled from bottom friction, which has important implications on previous results regarding the dynamics of a partially mixed estuary. *Geyer et al.* [2000] suggested that estuarine circulation depended merely on the intensity of bottom-generated turbulence and proposed that the residual flow could be modeled without any knowledge of the vertical eddy viscosity. However, the results of this investigation showed that elevated near-surface vertical eddy viscosity values can dominate in some locations across the estuary. This finding underscores the need for suitable representations of lateral processes and spatially varying vertical eddy viscosities for appropriate understanding of estuarine circulation.

5. Conclusions

The main message of this investigation was that lateral circulation is linked to near-surface vertical mixing appearing during the ebb phase throughout the fortnightly cycle. During neap tide conditions, near-surface instabilities were associated with the straining of lateral density gradients, set up by the influence of Coriolis effects confining less-dense water on the right side of the transect. Spring tide observations showed similar results from the channel slope to the southern shoal. However, the shear straining term combined with the density straining term to influence near-surface mixing between the channel and channel slope. Such structure of straining-related processes highlighted lateral and fortnightly variability. These results indicated that near-surface mixing is important and can develop from mechanisms decoupled from bottom friction. Therefore, vertical mixing can indeed exhibit different vertical structures across the estuary.

Appendix A

This appendix describes uncertainties from estimating TKE dissipation rates, ε . Ideally, multiple successive profiles collected at each station could be averaged together in spectral space (spectral smoothing), which

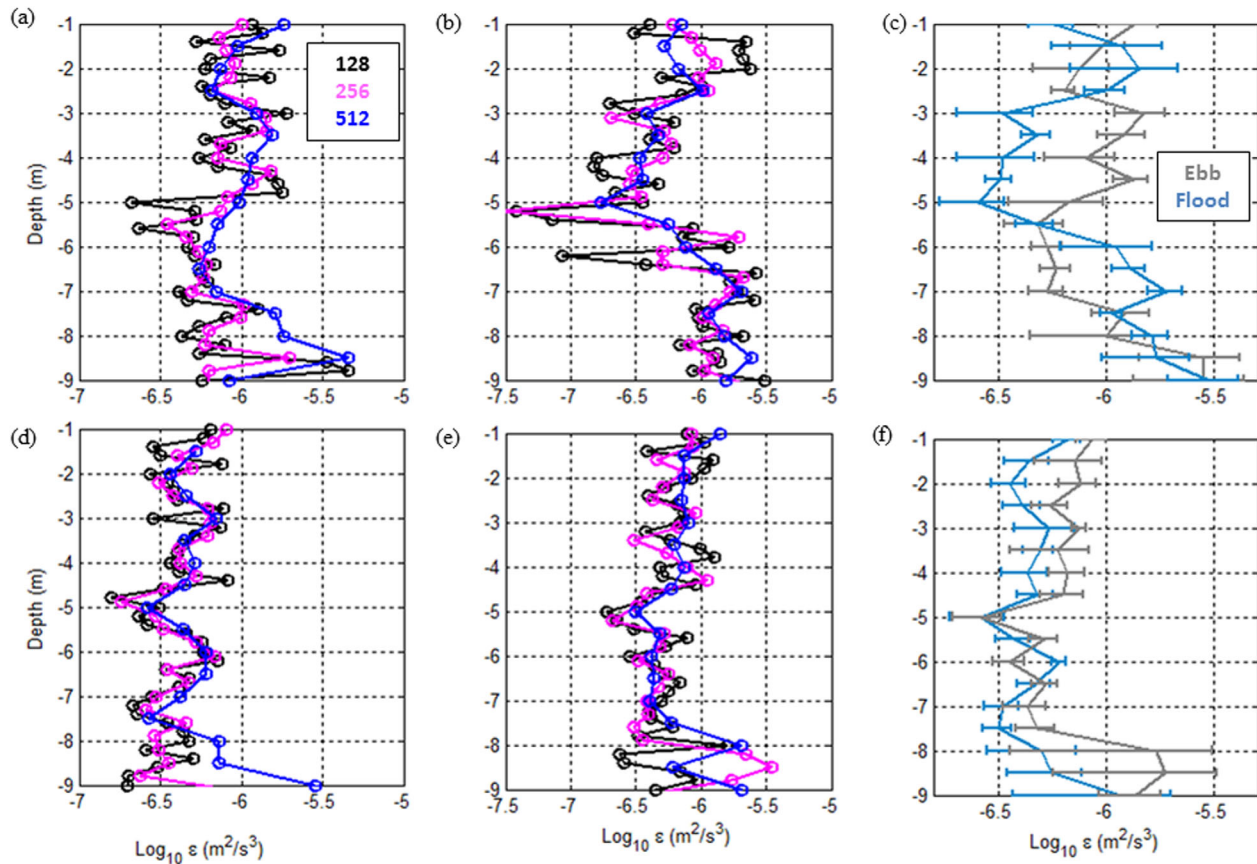


Figure A1. Neap tide: (a) ebb phase averaged ε profiles using 128 (black), 256 (magenta), and 512 (blue) scans per segment, (b) flood phase averaged ε profiles, (c) ebb (gray), and flood (blue) phase averaged bootstrapped mean and 95% confidence limits. Spring tide: (d) flood phase averaged ε profiles using 128 (black), 256 (magenta), and 512 (blue) scans per segment, (e) ebb phase averaged ε profiles, (f) ebb (gray), and flood (blue) phase averaged bootstrapped mean and 95% confidence limits.

would provide uncertainty bounds. However, this sampling method could not be implemented during data collection because of time constraints related to rapidly changing currents at all stations sampled. The temperature gradient data must be segmented into statistically stationary segments for the measured spectrum to resemble the Batchelor spectrum [Luketina and Imberger, 2001]. Therefore, it is optimal to choose a segment size that reflects homogeneous turbulence within a segment. Shorter segment sizes result in a noisier profile and less of the temperature gradient spectrum is resolved [Steinbeck et al., 2009].

A sensitivity analysis was conducted to test the influence of stationary segment sizes in estimating ε during different phases of the fortnightly and intratidal cycles. We estimated ε for the channel location (station 2) throughout the tidal cycle during both spring and neap tide using three segment sizes: 128, 256, and 512 scans, which represent roughly 13, 26, and 51 cm bins. The neap tide results are plotted in Figures A1a–A1c, which displays the ebb phase averages (Figure A1a) and flood phase averages (Figure A1b). Uncertainties associated with using 128, 256, and 512 scans per segment were estimated using the bootstrap method, where 95% confidence intervals were determined for each profile [Efron and Gong, 1983]. These values were then averaged over ebb and flood phases to yield a single profile (Figure A1b). This was also conducted during spring tide, where flood averages are presented in Figure A1d, ebb averaged are presented in Figure A1e and the uncertainties are plotted in Figure A1f.

The results of this analysis showed that the 128 scans per segment profiles were noisier than the 256 scans per segment profiles, as expected. However, 256 scans per segment yielded similar, yet smoother values. The 512 scans per segment tended to overestimate the values during more stratified conditions (neap tide) and near the bottom. The uncertainty between segment sizes was also largest during more stratified conditions, such as neap tide and the ebb phase. The Ozmidov length scale represents the largest length scale of an eddy before it is deformed by stratification, where scales are limited by greater stratification. Using

segment sizes that are larger than this length scale could contain multiple eddies, leading to an overestimation in ε . The tradeoff in using smaller segment sizes is that they tend to be noisier, but give a higher vertical resolution. Near the bottom, ε was the largest and using the smaller segment sizes likely resulted in the underestimation of ε . It would be ideal to implement an adaptive segmenting algorithm that would use varying segments through the water column (between mixed and stratified regions); however, *Luketina and Imberger* [2001] reported biases in such algorithms. Overall, this sensitivity analysis supported that 256 scans per segment was optimal for this analysis, with typical uncertainties of less than half an order of magnitude during weaker stratification.

Acknowledgments

This project was funded by the National Science Foundation project (OCE-0825826, OCE-0825833, and OCE-0825876). The authors would like to thank Jim O'Donnell specially for his generous help with the SCAMP data processing. Additionally, the authors would like to thank George Burnard, the captain of the boat, and Amy Waterhouse, Chloe Winant, Peng Cheng, Sabrina Parra, and Dove Guo for their contributions during fieldwork. The data, processing code, and figures used in this paper are available through the corresponding author: Huguenard.kimberly@gmail.com.

References

- Batchelor, G. K. (1959), Small-scale variation of convected quantities like temperature in turbulent fluid, Part 1. General discussion and the case of small conductivity, *J. Fluid Mech.*, *5*, 113–133.
- Baumert, H. Z., and H. Peters (2009), Turbulence closure: Turbulence, waves and the wave-turbulence transition—Part 1: Vanishing mean shear, *Ocean Sci.*, *5*, 47–58.
- Chant, R. J. (2010), Estuarine secondary circulation, in *Contemporary Issues in Estuarine Physics*, edited by A. Valle-Levinson, pp. 100–124, Cambridge Univ. Press, N. Y.
- Collignon, A., and M. Stacey (2013), Turbulence dynamics at the shoal-channel interface in a partially stratified estuary, *J. Phys. Oceanogr.*, *43*, 970–989, doi:10.1175/JPO-D-12-0115.1.
- Efron, B., and G. Gong (1983), A leisurely look at the bootstrap, the jackknife and cross-validation, *Am. Stat.*, *37*, 36–48.
- Geyer, R. W., M. E. Scully, and D. K. Ralston (2008), Quantifying vertical mixing in estuaries, *Environ. Fluid Mech.*, *8*, 495–509.
- Geyer, W. G., J. H. Trowbridge, and M. M. Bowen (2000), The dynamics of a partially mixed estuary, *J. Phys. Oceanogr.*, *30*, 2035–2048.
- Huijts, K. M. H., H. M. Schuttelaars, H. E. de Swart, and A. Valle-Levinson (2006), Lateral entrainment of sediment in tidal estuaries: An idealized model study, *J. Geophys. Res.*, *111*, C12016, doi:10.1029/2006JC003615.
- Ilicak, M., T. M. Ozgokmen, H. Peters, H. Z. Baumert, and M. Iskandarani (2008), Performance of two-equation turbulence closures in three-dimensional simulations of the Red Sea overflow, *Ocean Modell.*, *24*, 123–139.
- Jay, D. A., and J. D. Musiak (1994), Particle trapping in estuarine tidal flows, *J. Geophys. Res.*, *99*, 20,445–20,461.
- Joyce, T. M. (1989), In situ “calibration” of ship-board ADCPs, *J. Atmos. Oceanic Technol.*, *6*, 169–172.
- Kay, D. J., and D. A. Jay (2003), Interfacial mixing in a highly stratified estuary: 1. Characteristics of mixing, *J. Geophys. Res.*, *108*(C3), 3072, doi:10.1029/2000JC000252.
- Lacy, J., M. T. Stacey, J. R. Burau, and S. G. Monismith (2003), The interaction of lateral baroclinic forcing and turbulence in an estuary, *J. Geophys. Res.*, *108*(C3), 3089, doi:10.1029/2002JC001392.
- Lerczak, J. A., and W. R. Geyer (2004), Modeling the lateral circulation in straight, stratified estuaries, *J. Phys. Oceanogr.*, *34*, 1410–1428.
- Li, M., L. Zhong, and W. C. Boicourt (2005), Simulations of Chesapeake Bay estuary: Sensitivity to turbulence mixing parameterizations and comparison with observations, *J. Geophys. Res.*, *110*, C12004, doi:10.1029/2004JC002585.
- Li, M., P. Cheng, R. Chant, A. Valle-Levinson, and K. Arnott (2014), Analysis of vortex dynamics of lateral circulation in a straight tidal estuary, *J. Phys. Oceanogr.*, *44*(10), 2777–2793, doi:10.1175/JPO-D-13-0212.1.
- Luketina, D. A., and J. Imberger (2001), Determining turbulent kinetic energy dissipation from Batchelor curve fitting, *J. Atmos. Oceanic Technol.*, *18*, 100–113.
- Nihoul, J. C. J., and B. M. Jamart (Eds.) (1987), *Three-Dimensional Models of Marine and Estuarine Dynamics*, pp. 1–34, Elsevier, Amsterdam.
- Osborn, T. R. (1980), Estimates of the local rate of vertical diffusion from dissipation measurements, *J. Phys. Oceanogr.*, *10*, 83–89.
- Peters, H. (1997), Observations of stratified turbulent mixing in an estuary: Neap-to-spring variations during high river flow, *Estuarine Coastal Shelf Sci.*, *45*, 69–88.
- Peters, H., H. Baumert, and J. P. Jacob (2005), Partially mixed estuaries: The Hudson River, in *Marine Turbulence, Theories, Observations and Models*, edited by H. Baumert, J. Simpson, and J. Sündermann, pp. 324–333, chap. 39, Cambridge Univ. Press, Cambridge, U. K.
- Ruddick, B., A. Anis, and K. Thompson (2000), Maximum likelihood spectral fitting: The Batchelor spectrum, *J. Atmos. Oceanic Technol.*, *17*, 1541–1555.
- Shen, J., and J. Lin (2006), Modeling study of the influences of tide and stratification on age of water in the tidal James River, *Estuarine Coastal Shelf Sci.*, *68*, 101–112.
- Sinha, P. C., G. K. Jena, I. Jain, A. D. Rao, and M. L. Husain (2010), Numerical modelling of tidal circulation and sediment transport in the Gulf of Khambhat and Narmada Estuary, West Coast of India, *J. Sci. Technol.*, *18*, 293–302.
- Souza, A. J. (2013), On the use of the Stokes number to explain frictional tidal dynamics and water column structure in shelf seas, *Ocean Sci.*, *9*, 391–398.
- Steinbeck, J. V., M. T. Stacey, M. A. McManus, O. M. Cheriton, and J. P. Ryan (2009), Observations of turbulent mixing in a phytoplankton thin layer: implications for formation, maintenance, and breakdown, *Limnol. Oceanogr.*, *54*(4), 1353–1368.
- Tjernstrom, M. (1993), Turbulence length scales in a stably stratified free shear flow analyzed from slant aircraft profiles, *J. Appl. Meteorol.*, *32*, 948–963.
- Turner, J. S. (1973), *Buoyancy Effects in Fluids*, Cambridge Univ. Press., Cambridge, U. K.
- Valle-Levinson, A. (2008), Density-driven exchange flow in terms of the Kelvin and Ekman numbers, *J. Geophys. Res.*, *113*, C04001, doi:10.1029/2007JC004144.
- Valle-Levinson, A., K. C. Wong, and K. M. M. Lwiza (2000), Fortnightly variability in the transverse dynamics of a coastal plain estuary, *J. Geophys. Res.*, *105*, 3413–3424.